

MATERIALS SCIENCE

Spatially resolved structural order in low-temperature liquid electrolyte

Yujun Xie^{1,2,3†}, Jinyang Wang^{3,4†}, Benjamin H. Savitzky², Zheng Chen⁵, Yu Wang³, Sophia Betzler³, Karen Bustillo², Kristin Persson^{6,7}, Yi Cui⁴, Lin-Wang Wang^{3‡}, Colin Ophus^{2*}, Peter Ercius^{2,3*}, Haimei Zheng^{3,7*}

Determining the degree and the spatial extent of structural order in liquids is a grand challenge. Here, we are able to resolve the structural order in a model organic electrolyte of 1 M lithium hexafluorophosphate (LiPF₆) dissolved in 1:1 (v/v) ethylene carbonate:diethylcarbonate by developing an integrated method of liquid-phase transmission electron microscopy (TEM), cryo-TEM operated at -30°C , four-dimensional scanning TEM, and data analysis based on deep learning. This study reveals the presence of short-range order (SRO) in the high-salt concentration domains of the liquid electrolyte from liquid phase separation at the low temperature. Molecular dynamics simulations suggest the SRO originates from the Li⁺-(PF₆⁻)_n ($n > 2$) local structural order induced by high LiPF₆ salt concentration.

INTRODUCTION

Understanding structural order across a multitude of length scales is central to controlling the physical properties of materials. Atomic correlations in many amorphous solids are found in the short-range order (SRO) regime of less than 5 Å. Mounting experimental evidence has confirmed the existence of SRO and its strong influence on electrical conduction (1–3), ion transport (4, 5), mechanical strength (6–8), and crystallization processes (9, 10). However, although direct imaging of the SRO using transmission electron microscopy (TEM) has been realized in solids (1, 8, 9), its observation in liquids at comparable spatial scales has not been achieved despite the structural order being observed in liquids using x-rays over many decades ago (11). The challenge is, in part, due to the high sensitivity of the liquid to the electron beam and weak scattering from low-atomic number elements that typically constitute the liquids (see fig. S1) (12). To date, investigating the structure of liquids is still limited to scattering measurements averaged over relatively large volumes of material (13, 14). The lack of information on the degree and spatial extent of the structural order in liquids hinders elucidation of the microscopic structures and of the formation conditions of SRO, which often influence critical processes in liquid solutions such as nucleation, self-assembly, and phase separation especially at thermochemical nonequilibrium states (15, 16).

Liquid electrolytes in Li-ion batteries represent one important class of materials whose macroscopic properties are closely related

to the microscopic structures of its components, i.e., salt ions and solvent molecules (17). For instance, in high-salt concentration electrolytes, salt cations and anions tend to associate to a high degree and form superstructures such as aggregates, thereby improving interfacial stability and Coulombic efficiency; this superstructure also leads to the lowered ionic conductivity and increased viscosity that are similar to the low-temperature performance of Li-ion battery below 0°C (18–20). These findings highlight the need to understand the structural order at the molecular level and its spatial extent at the mesoscale. Furthermore, the formation conditions of structural order are essential for rational design of functional electrolytes under various working conditions (4, 21). The ability to characterize the underlying structure of liquid electrolytes at high spatial resolution is crucial for elevating future battery performance.

Direct imaging of the structural order of volatile liquid systems has not been achieved, arising from a number of technical challenges. Conventional techniques such as atomic force microscopy were used to estimate the local orientational order on the surface of an electrolyte as a function of salt concentration (22). The structural order in the form of aggregates was also demonstrated using x-ray and neutron scattering methods. From these scattering methods, the radial distribution function (RDF) suggested that the characteristic correlation length was less than a few angstroms (23, 24). Raman spectroscopic and nuclear magnetic resonance techniques have frequently been used to reveal the structural evolution as a function of temperature and salt concentration (25). However, the evidence is mostly inferred from a relatively large sample volume and lacks spatial resolution on the nanometer scale. The emerging four-dimensional scanning TEM (4D-STEM) technique that uses a highly controllable convergent beam has recently revealed structural order in solids at the level of molecules and nanoscale domains (26–28). Nonetheless, it has not been introduced to liquid samples despite the sufficient scattering efficiency and spatial resolution in principle. Moreover, cryo-TEM has become an important technique for investigating aqueous materials at high resolution by rapidly freezing the pristine structure of the material from ambient conditions (29, 30). However, ideally, one would want to

¹Department of Nuclear Engineering, University of California, Berkeley, Berkeley, CA 94720, USA. ²National Center for Electron Microscopy, Molecular Foundry, Lawrence Berkeley National Laboratory, Berkeley, CA 94720, USA. ³Materials Sciences Division, Lawrence Berkeley National Laboratory, Berkeley, CA 94720, USA. ⁴Department of Materials Science and Engineering, Stanford University, Palo Alto, CA 94305, USA. ⁵Department of Mechanical Engineering and Materials Science, Yale University, New Haven, CT 06511, USA. ⁶Energy Technologies Area, Lawrence Berkeley National Laboratory, Berkeley, CA 94720, USA. ⁷Department of Materials Science and Engineering, University of California, Berkeley, Berkeley, CA 94720, USA.

[†]These authors contributed equally to this work.

[‡]Present address: State Key Laboratory of Superlattices and Microstructures, Institute of Semiconductors, Chinese Academy of Science, Beijing 100083, China.

*Corresponding author. Email: clophus@lbl.gov (C.O.); percius@lbl.gov (P.E.); hmzheng@lbl.gov (H.Z.)

image the organic electrolyte in the native “wet” state instead of merely the quenched solid at a temperature set by the cryogen [-180°C for liquid nitrogen (LN_2)] to allow simultaneous access to the liquid and solid phases and avoid potential structural changes during the vitrification process (31, 32). Toward this end, we have developed an integrated experimental method depicted in Fig. 1A to measure structural order in liquid electrolytes at low temperatures that is relevant to battery applications. Using the heating capability of a cryo-TEM holder, we have achieved temperatures from -170°C to -5°C by balancing cryogen cooling with Joule heating (table S1). Organic liquids typically exhibit a liquid state at a wide range of temperatures, and this technique allows the liquid electrolyte to maintain the liquid phase. A secondary benefit to the reduced temperature is that electron beam damage is mitigated because of the reduced diffusion of beam ionization products (12). We then applied liquid-phase TEM techniques to maintain the volatile liquids under vacuum. Now, most liquid cell experiments are based on imaging with mass thickness and/or phase contrast, requiring a large input radiation dose (33). However, a large radiation dose is incompatible with radiation-sensitive materials, such as organic liquids, even at low temperatures. Furthermore, organic electrolytes have weak contrast for real-space imaging; the reciprocal space RDF measurements acquired in this work made efficient use of the incident electron dose. Therefore, by combining with the 4D-STEM technique, a series of 2D diffraction patterns was acquired from a set of 2D scanning positions with a spatially localized electron probe (~ 2 nm in diameter) to minimize beam damage (27).

RESULTS

The model organic liquid for this study is the widely used commercial electrolyte 1 M lithium hexafluorophosphate (LiPF_6) dissolved in 1:1 (v/v) ethylene carbonate (EC) and diethyl carbonate (DEC) (1

M LiPF_6 in 1:1 EC:DEC). Approximately $1\ \mu\text{l}$ of 1 M LiPF_6 in 1:1 EC:DEC was loaded into a carbon-film liquid cell, forming a thin liquid layer sandwiched between two thin carbon membranes. After mounting the liquid cell on a Gatan 636 cryo-holder and loading it into the TEM, the temperature of the liquid specimen was stabilized at -30°C , allowing the liquid to reach the designated equilibrium phase (fig. S3). A high-angle annular dark-field (HAADF) STEM image of the 1 M LiPF_6 in 1:1 EC:DEC with biphasic equilibria is shown in Fig. 1B. The inset shows a selected area diffraction pattern obtained from the bright region, confirming the expected existence of crystallized EC at this temperature (fig. S3) (34). According to the phase diagram, the rest of the dark domain likely remained in the liquid state (35), and a higher-resolution HAADF-STEM image from the dark area surrounded by solid EC showed at least two phases with different contrast (Fig. 1C). However, a single HAADF-STEM image is insufficient to determine the structure or composition of these phases.

To extract the accurate structural information, we performed 4D-STEM measurements in the liquid domain marked with a white dotted rectangle shown in Fig. 1C. Figure 1 (D to F) shows a representative subset of diffraction patterns acquired at the probe positions (marked with purple, orange, and blue boxes). A fraction of the diffraction patterns (purple box) indicates long-range order from the crystalline structure, which was not apparent in the low-resolution HAADF-STEM images. These lattice reflections always occur within the regions that exhibit brighter contrast in HAADF-STEM image. In contrast, the two remaining types of patterns (marked orange and blue boxes) both exhibited three diffuse rings centered at $q_1 = 0.23\ \text{\AA}^{-1}$, $q_2 = 0.45\ \text{\AA}^{-1}$, and $q_3 = 0.82\ \text{\AA}^{-1}$, which imply their similar disordered structures despite the apparent contrast in HAADF-STEM images (fig. S4). Note that the faint halos are similar to the diffraction pattern from quenched 1 M LiPF_6 in 1:1 EC:DEC electrolytes previously presented, which supports the hypothesis that it is a noncrystalline state (29).

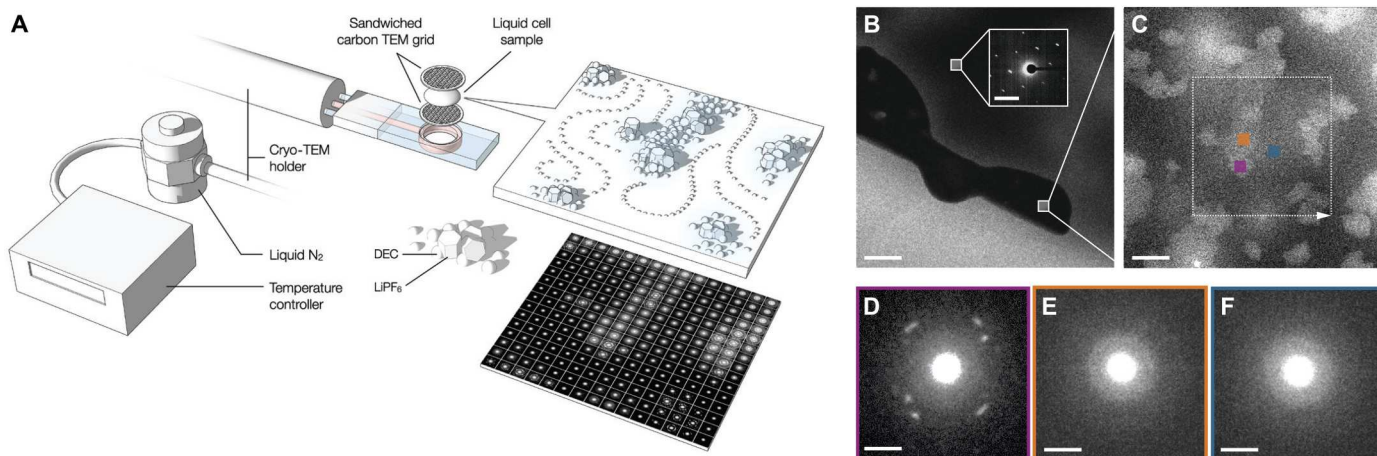


Fig. 1. Schematic illustration of the hybrid method and high-angle annular dark-field STEM images of 1 M LiPF_6 in 1:1 ethylene carbonate:diethyl carbonate. (A) A combination of liquid cell and modified cryo-TEM technique enables the capability to characterize highly beam-sensitive liquid organic electrolyte 1 M LiPF_6 in 1:1 ethylene carbonate (EC):diethyl carbonate (DEC) at -30°C . 4D-STEM applies a focused convergent beam scanning over the area of interest, and a full diffraction pattern is acquired for each real-space probe location (x, y), with a step size large enough to prevent the sample from damaging yet sampling neighboring positions. (B) High-angle annular dark-field (HAADF) STEM image of 1 M LiPF_6 in 1:1 EC:DEC shows biphasic equilibria at -30°C . Inset is the representative diffraction pattern obtained from the apparent crystals showing Bragg peaks associated with EC. Scale bars, $5\ \mu\text{m}$ and $0.25\ \text{\AA}^{-1}$. (C) Higher-resolution HAADF-STEM image from the dark region shows at least two phases with different contrast of brightness. Scale bar, $250\ \text{nm}$. (D to F) Examples of three types of diffraction patterns acquired using 4D-STEM from the corresponding scan positions labeled in purple, orange, and blue. Scale bars, $0.25\ \text{\AA}^{-1}$.

However, diffraction patterns from the two regions are very similar, which hinders measurements of subtle structural differences. Thus, we used a deep learning classification process to classify each radial sum of diffraction patterns (detailed in Materials and Methods). Three structurally distinct phases were identified in Fig. 2 (A to E). Phase I represents the strongly diffracting crystalline regions with discrete lattice reflections. These peaks are identified as trigonal LiPF_6 polycrystals with grain size of <50 nm via automatic indexing methods (fig. S5 and Materials and Methods) (36). Phases II and III are differentiated on the basis of the first sharp diffraction peak corresponding to scattering at $q_1 = 0.23 \text{ \AA}^{-1}$; we found it statistically narrower and of higher amplitude in the radial intensity profile of class II. Figure 2F shows the reconstructed phase map. While phases II and III are separated and spatially extended up to micrometer, phase I is found to be embedded in phase II. This is consistent with the reconstructed virtual dark-field image shown in Fig. 2G, in which the brightness is a function of scattered intensity. Therefore, we believe the contrast in brightness of the two amorphous phases shown in Fig. 1C manifested because of a difference in structural order, as revealed by the scattering intensity of the q_1 ring in phases II and III.

The apparent liquid-liquid separation of phases II and III is unexpected and in contrast to the common assumption that liquid electrolytes are homogeneous. Although several studies have implied that such anomalous phenomenon is a dense liquid phase in a saturated solution or at supercooled regime, it has not been structurally characterized down to the nanoscale (15, 16). Dense liquid phase is now regarded as the possible precursor to crystalline phases (37). As all the LiPF_6 polycrystals are observed within phase II shown in Fig. 2F, we hypothesize that phase II is the dense liquid phase before the LiPF_6 precipitation due to the decrease of solubility upon cooling. In other words, phase II should contain a higher density of LiPF_6 . In this regard, the increased brightness of phase II in Fig. 1C may be attributed to the increased density. However, it does not account for the increased first sharp diffraction peak intensity of phase II in comparison with phase III. The presence of a dense liquid phase is consistent with our theoretical calculations.

The concept of first sharp diffraction peak has been known as the signature for qualitative analysis of the structural ordering, of which

position and intensity indicate the molecular-scale architectures and degree of the ordering, respectively, such as the SRO in glasses and polymers (38, 39). The first sharp diffraction peak of phases II and III located at $q_1 = 0.23 \text{ \AA}^{-1}$ is equal to a correlation length of 4.34 \AA . Such a large distance indicates a structural ordering extending beyond the nearest neighbor atom in the electrolyte (table S1). In addition, although it is tempting to believe that the increased intensity of the first sharp diffraction peak of phase II is the direct indication of SRO, it could not rule out other effects arising from the variation of thickness and density across the sample.

To gain further insight into the structural differences of the two phases, low-dose spectroscopic mapping by electron energy-loss spectroscopy (EELS) mapping was performed at -30°C [Fig. 3 (A to E) and Materials and Methods]. By analyzing the fine structure of the carbon K -edge, we observe distinct C—H bonds at 287 eV and C=O bonds at 291 eV, in agreement with the bonding environment of the DEC-based electrolyte (29). The uniform spatial distribution of the carbon elemental map, constructed by summing the carbon K -edge at each probe position across the dark and bright regions, rules out substantial changes of sample thickness of the organic liquid. In addition, the spectroscopic maps of lithium and fluorine are in accordance with the hypothesis of dense liquid phase as both lithium K -edge and fluorine K -edge, implying a higher concentration of LiPF_6 within the brighter region. The bright region was found to have approximately two to four times higher lithium concentration than that of the dark domain (fig. S6). Although lithium does not scatter heavily and would not contribute to the HAADF-STEM intensity, the spatial distribution of these elements in general agrees with the HAADF-STEM intensity in Fig. 3B, suggesting their correlations with the intensity of the q_1 diffraction ring. Although in-depth quantitative analysis cannot be conducted because of the low signal-to-noise ratio of the EELS signal and the difficulty of performing STEM-EELS and 4D-STEM on the same regions due to beam damage, the findings are consistent with the hypothesis that phase II is a dense liquid phase with LiPF_6 , possibly close to the saturated concentration level for precipitation. Thus, we conclude that the increased first sharp diffraction peak intensity results from

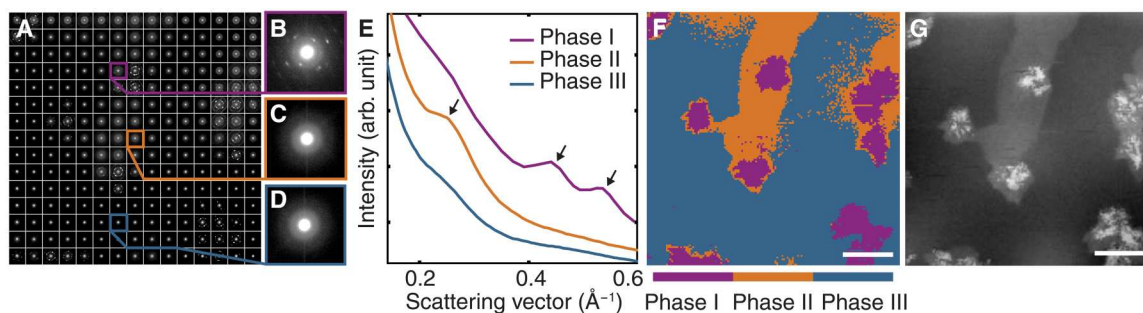


Fig. 2. Deep learning analysis of 4D-STEM datasets. (A) Sample diffraction patterns in a 150×150 pixel 4D-STEM dataset. Each shown diffraction pattern is a sum of 10×10 diffraction frames to improve contrast for publication. (B to D) Example diffraction patterns from the location marked with blue, orange, and purple boxes. (E) A visualization of the radial sum. To show features, what is shown is a sum of 100 diffraction patterns, although the analysis treated each frame separately, preserving the 10-nm step size. Three phases were classified by the neural network model. Phase I (purple) represents the crystalline phases, in which the black arrows marked the corresponding Bragg peaks of LiPF_6 . Phase II (orange) and phase III (blue) are from the diffraction patterns with amorphous rings, which correspond to the bright and dark regions, respectively. The black arrow in phase II indicates the stronger scattered intensity at 0.23 \AA^{-1} . arb. unit, arbitrary unit. (F) A reconstructed phase mapping based on three phases. (G) A reconstructed virtual dark-field image measuring the brightness of an annular ring shows identical morphologies to the phase mapping. Scale bar, 250 nm.

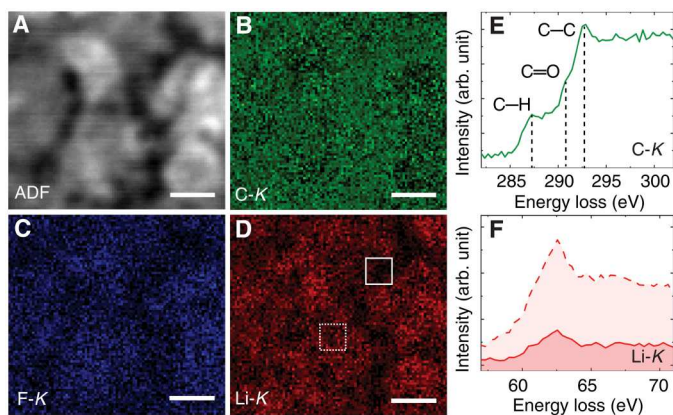


Fig. 3. STEM-EELS of 1 M LiPF₆ in 1:1 EC:DEC electrolyte at -30°C . (A) ADF-STEM image of a representative region with liquid-liquid phase separation. Scale bar, $1\ \mu\text{m}$. (B to D) The EELS elemental mapping of the *K*-edge of carbon, fluorine, and lithium. Scale bars, $250\ \text{nm}$. (E) The corresponding STEM-EELS fine structures of the summed carbon *K*-edges from (B). Distinct carbon bonds are labeled. (F) The representative STEM-EELS fine structures of the lithium *K*-edges from the white box and white dotted box in (D), respectively.

stronger order in phase II at short-range regime with a correlation length of $4.3\ \text{\AA}$.

To understand the structural origin and the formation mechanism of SRO in the high-concentration electrolyte, we performed molecular dynamics (MD) simulations of 1 and 4 M LiPF₆ in DEC solutions (see details in Materials and Methods). The resulting overall molecular structures show a qualitative difference between these two concentrations, namely, the prevalence of SRO structures in the 4 M solution and the lack thereof in the 1 M solution (Fig. 4A), in agreement with the experimental findings. The characteristic length of SRO $r_{\text{SRO}} = 4.2\ \text{\AA}$, corresponding to the first sharp diffraction peak at $0.23\ \text{\AA}^{-1}$, matches the mean distance of the first peak in the P-F RDF (Fig. 4B and fig. S7). This result suggests that a particular spatial arrangement of neighboring PF₆[−] ions is responsible for the SRO formation in the 4 M solution. Further analysis reveals that nearly all PF₆[−] anions are directly linked with one or more Li⁺ ions in the 4 M solution, forming contact ion pairs (CIPs) and aggregates (Fig. 4C), consistent with previous findings for high-concentration salt solutions (40–42). These solvation structures are distinguished by ordering on two different length scales. Over short distances ($<1\ \text{nm}$), the strong P-F correlations at 4.2 and $6\ \text{\AA}$ (Fig. 4B) are due to the neighboring pair of PF₆[−] ions within the same Li⁺(PF₆[−])_{*n*} ($n > 2$) structural unit (Fig. 4C). Such units are found in 76% of the Li⁺ primary solvation shells in the 4 M solution, in which most of $n = 2$ units and almost all $n = 3$ and $n = 4$ units contain SRO (Fig. 4D and fig. S7). Over longer length scales ($>1\ \text{nm}$), multiple Li⁺(PF₆[−])_{*n*} units are connected and repeated in space to form polymer-like aggregates with lengths reaching nanometers and containing up to ~ 200 Li⁺ and PF₆[−] ions, respectively (Fig. 4C and fig. S8). In contrast, in the 1 M solution, 70% of Li⁺ ions are fully solvated by four DEC molecules, and most of the remaining Li⁺ (20%) are coordinated with three DEC molecules and one PF₆[−] ion, forming individual CIPs (fig. S7). Additional MD simulations of LiPF₆:DEC with various salt concentrations indicate that the onset of SRO occurs at around 1.9 M. Furthermore, the P-F correlation does not change

qualitatively under room temperature compared with under $T = 240\ \text{K}$ (fig. S9). These findings highlight the direct connection between the Li⁺(PF₆[−])_{*n*} ($n > 2$) units and the SRO in the electrolyte and the importance of high salt concentration as a necessary condition for the emergence of such units.

The potential of mean force (PMF) of salt ion separation provides a more quantitative picture of the ion cluster formation process in regular- and high-concentration electrolytes. As shown in fig. S10, the ionic binding between Li⁺ and PF₆[−] is more thermodynamically favorable in 4 M LiPF₆ in DEC solution ($-1.20\ \text{kcal/mol}$) than in 1 M solution ($-0.88\ \text{kcal/mol}$), as fewer DEC molecules produce weaker screening of electrostatic attractions between the counterions. This leads to a preference for forming CIPs over solvent-separated ion pairs in the 4 M solution, as indicated by the lack of a well-defined second valley in the Li-P PMF. This behavior is in contrast to the 1 M solution, where a second valley around $\sim 8\ \text{\AA}$ is discernible. The combined effect of the thermodynamic preference for CIP formation and the dense population of salt ions in the 4 M solution eventually leads to a cascade of PF₆[−]-Li⁺-PF₆[−] bonding, which is the chemical basis of aggregate formation. The Li⁺(PF₆[−])_{*n*} ($n > 2$) units found in the 4 M solution serve as the building blocks of such aggregates, which can be seen as the precursors of crystalline LiPF₆ precipitates, where each Li⁺ ion octahedrally coordinates with six PF₆[−] ions.

DISCUSSION

The observation of SRO in high-concentration electrolytes may define a series of macroscopic parameters such as ion ionic conductivity, ionic transport mode, and viscosity. The phase separation can be a potential design principle of improved electrochemical performance including interphase stability (43, 44). For example, a biphasic electrolyte can have one phase with high reactivity toward an electrode, which produces a known, functional, and passivating interface combined with another phase with lower reactivity and higher conductivity (45). As another example, some of the high-concentration electrolytes such as the water-in-salt electrolytes have shown not only beneficial interfacial reactivity, increasing the effective voltage window of water battery systems by more than 1 V, but also prevalence of nanodomains with an unexpectedly high Li conductivity and transference number due to the existence of “Li-solvent freeways” within a matrix of high anion domains (46). Beyond that, the approach using liquid-phase 4D-STEM techniques with machine learning data analysis could enable multiscale structural characterization of phase transitions in liquid and perhaps address the mystery of solid-liquid interface on the microscopic level.

MATERIALS AND METHODS

Materials and liquid cell fabrication

Commercially available 1 M LiPF₆ in 1:1 EC:DEC (battery grade; Sigma-Aldrich) was used as received. Both are stored in argon-filled glove box (oxygen content less than 10 parts per million). Thin carbon film (10 nm, 400 mesh)-supported copper grids were purchased from Electron Microscopy Sciences. The fabrication of liquid cell was fabricated through a fast drop-casting method. Less than $1\ \mu\text{l}$ of solution is first drop-casted on one of the carbon grids and then quickly sandwiched together with another

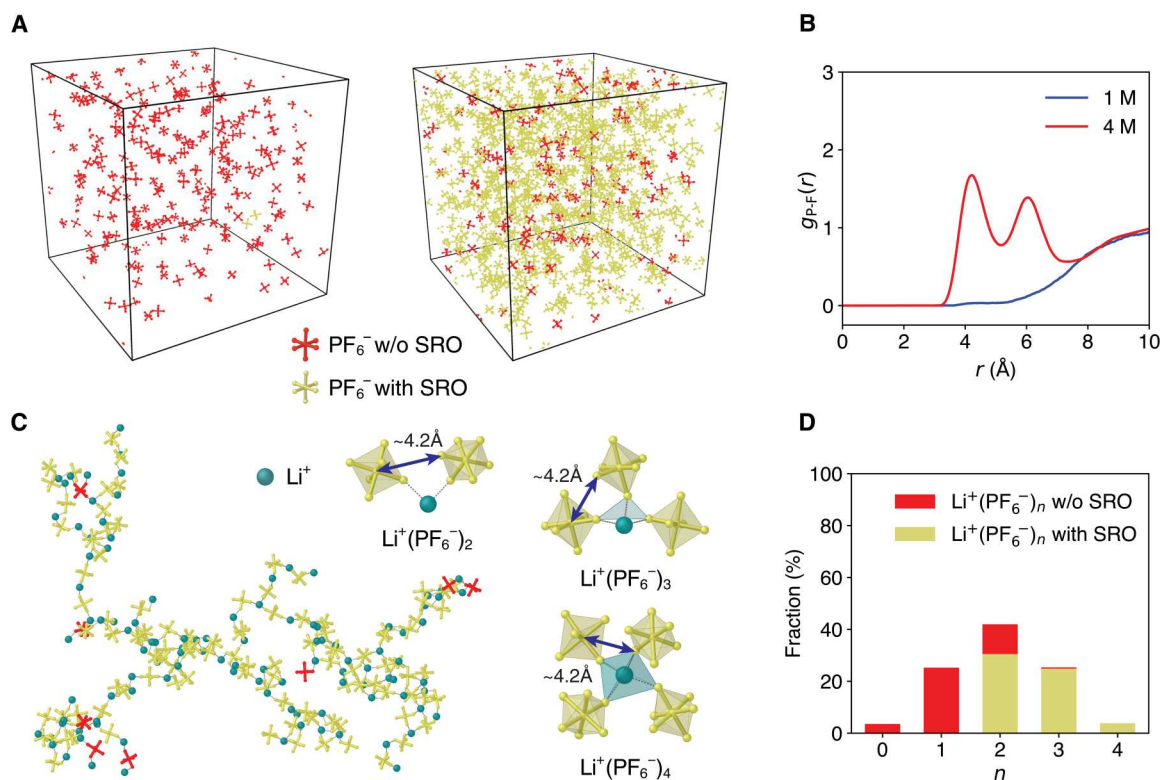


Fig. 4. Structural analysis of MD simulations. (A) Snapshots of structural configuration of 1 M (left) and 4 M (right) LiPF₆ in DEC systems. Red, PF₆⁻ without SRO. Gold, PF₆⁻ with SRO. Li⁺ and DEC are hidden for clarity. (B) The P-F RDF. The first peak of the 4 M solution corresponds to the SRO. (C) A view of an aggregate containing 107 Li⁺ and 115 PF₆⁻, and three representative local structural units Li⁺(PF₆⁻)₂, Li⁺(PF₆⁻)₃, and Li⁺(PF₆⁻)₄ from the 4 M LiPF₆:DEC system. One possible SRO-containing PF₆ pair is schematically marked with an arrow in each unit. Cyan, Li⁺. (D) Fraction of SRO-containing/total Li⁺(PF₆⁻)_n units in the 4 M LiPF₆:DEC system.

fresh carbon grid. The specimen was gently mounted on a Gatan 636 cryo-TEM holder.

Cryo-TEM setup for various low temperatures

Various low temperatures, from -180° to -5°C , were achieved by using the temperature controller with the Gatan 636 cryo TEM holder. The liquid cell specimen was loaded in the holder and inserted into the TEM at room temperature. The LN₂ dewar on the holder was filled with LN₂ to cool down the liquid cell specimen while sourcing enough current (0 to 0.75 Å) to drive the heating element in the tip of the TEM holder (table S1). Therefore, the sample temperature directly decreased from room temperature to the set temperature. Liquid cell specimen temperature is monitored by thermocouple located close to the specimen until it reached the targeted temperature at about 0.3°C/s, which takes about 15 min to stabilize at $\pm 2^{\circ}\text{C}$. The drift rate is calculated to be about 3.2 Å/s from fig. S11, which changes the actual step size only slightly for the fast 4D-STEM measurement.

TEM measurement

All 4D-STEM measurements were carried out using a Gatan Orius charge-coupled device on a FEI TitanX microscope at 300 kV operated in microprobe STEM mode. Convergence semi-angle α is set to be 0.48 mrad with camera length of 300 mm. The Gaussian-shaped probe size was measured to be 2 nm at full width at half-maximum (FWHM). We did not use beam stop to avoid masking any diffraction spots and do the realignment of the diffraction

patterns (DPs) due to the shift of the beams during scan. Having a nonoverlapping small spot on the diffraction is preferred for later template matching because of the sharp difference of intensity contrast between spots and background.

After the liquid cell specimen stabilized at the targeted temperature, we carefully located the region of interest in STEM diffraction mode with fast acquisition time of ~ 0.5 s to minimize beam damage while having enough contrast, at which point we blanked the beam. The regions for 4D-STEM were determined semiblindly by moving the goniometer position with precise distance, for instance, 4 μm , to make sure that we are away from the damaged area. We then unblanked the beam followed immediately by launching the 4D-STEM acquisition process. 4D-STEM parameters were determined empirically to balance the signal-to-noise ratio on the diffraction pattern and the beam damage. We measured the probe size at FWHM to be approximately 2 nm. However, as the secondary electrons spread laterally, causing damage ahead of the probe, we used a step size of 10 nm to avoid destroying the next areas that had yet to be scanned. Acquisition time was set to be 50 ms, which is the fastest that our scripts can run the 4D-STEM acquisition. A step size of 10 nm was optimized to avoid damage from the previous scan position. However, we can estimate the electron dose ($e^{-}\text{\AA}^{-2}$) on the specimen using a general approach by averaging the dose over the entire scanned area (26). The calculation of dose is 140 ($e^{-}\text{\AA}^{-2}$) based on a beam current of 4.5 pA with a step size of 10 nm and acquisition time of 50 ms in this work. Typical HAADF-STEM images

correspond to a dose of 10^3 to $10^4 e^- \text{ \AA}^{-2}$, which are substantially higher than 4D-STEM measurements.

STEM-EELS measurements were acquired using a Gatan K3 direct-detection camera in the electron-counting mode using TEAM I at National Center of Electron Microscopy at Lawrence Berkeley National Laboratory under 300-keV electron beam. Characterization was performed with a C2 aperture of 50 μm , a probe current of 50 pA, a camera length of 400 mm, a pixel dwell time of 50 ms, and step size of 20 nm to minimize the beam damage and avoid destroying to the next areas that had yet to be scanned. EELS spectra were acquired with a high-resolution Gatan imaging filter (GIF Continuum 966) with a dispersion of 0.35 eV per channel. The electron dose applied during acquisition of the spectroscopic maps was below 500 $e/\text{\AA}$ to avoid mass loss and fine structure change.

Data processing

The 4D-STEM data were processed using py4DSTEM to extract the diffraction spot positions (28). The shift of the diffraction pattern is one of the main concerns due to the large scanned field of view and was measured as a function of probe x and y positions. We centered each diffraction pattern by setting each unscattered center disks to the original position where $(K_x, K_y) = 0$. Shift-corrected central disk was used as a template for matching all the scattered Bragg disk positions.

We processed the diffraction data from each real-space pixel into intensity curves as a function of the distance to center, which includes most of the diffraction information and avoids some measurement noise. The longest distance to the center of the intensity curve was 256 pixels, half of the original resolution (512 pixels), which can be represented as a multidimensional vector input for the model. First, we used unsupervised learning (here, K -means) to cluster the intensity curves with an estimate number of groups. Then, we randomly stratified a manageable sized group of pixels including all clusters (~1% of total 22,500 diffraction patterns) and manually labeled them on the basis of the original diffraction patterns and HAADF-STEM measurements by three researchers. The differentiated group size should be slightly fewer than the variable K , which is designed to avoid missing much structural information in the labeled data. If not, the process needed to restart from the clustering with a larger estimate for the groups number (K). The classified data were used as the training and validation data for a multiple-layer neural network model, and the trained model then classified the rest of the intensity curves. This method can be applied to multiple images of the same materials system at the same time, which results in less possibility of missing phases and enhanced overall classification efficiency by training one model for all images.

MD simulations

Classical MD simulations in this work were performed with the LAMMPS package (47). The all-atom optimized potentials for liquid simulations (OPLS-AA) force field (48) for LiPF_6 and DEC was used (49). The atomic partial charges of Li^+ and PF_6^- are scaled down by a factor of 0.8 to account for dielectric screening effect in DEC (50). For the 1 and 4 M LiPF_6 :DEC systems, the initial random structures were generated using PACKMOL (51, 52). The 1 M LiPF_6 :DEC system contains 1900 DEC molecules and 202 LiPF_6 molecules, and the 4 M LiPF_6 :DEC system contains 1600 DEC

molecules and 858 LiPF_6 molecules. For the LiPF_6 :DEC systems presented in the Supplementary Materials, the molecule numbers range from 20 LiPF_6 :380 DEC to 140 LiPF_6 :260 DEC. The simulation protocol is as follows: energy minimization, equilibration at 500-K temperature for 1 ns in NVT_ensemble, relaxation at 500 K for 1 ns inNPT ensemble, annealing to 240 K (300 K) for 2 ns in NPT ensemble, and equilibration at 240 K (300 K) for 5 ns in NPT ensemble. The production run was carried out at 240 K (300 K) temperature for 11 ns in NVT ensemble, of which the trajectories of the last 10 ns were used for data analysis. All the simulations used a time step of 1 fs and a pressure of 1 atm. The Nose-Hoover method is used to regulate the temperature and pressure, with a respective damping parameter of 0.2 and 1 ps.

The RDF $g(r)$ and the first solvation shell coordination numbers were calculated with the Python code MDAnalysis (53). The PMF was calculated directly from the time averaged RDF with the formula $\text{PMF}(r) = k_B T \ln \langle g(r) \rangle$, where k_B is the Boltzmann constant. The time averaging used snapshots taken every 50 ps to minimize time correlation effects. Structural analysis of salt ion clusters was carried out with custom code based on the breadth-first search algorithm, which iteratively searches for neighboring F atoms of Li^+ and neighboring Li^+ of F atoms within a cutoff of 2.5 \AA . Visualization of MD snapshots and local SRO units was performed with OVITO and CrystalMaker (54).

Supplementary Materials

This PDF file includes:

Figs. S1 to S12

Table S1

References

REFERENCES AND NOTES

1. A. Kumar, J. N. Baker, P. C. Bowes, M. J. Cabral, S. Zhang, E. C. Dickey, D. L. Irving, J. M. LeBeau, Atomic-resolution electron microscopy of nanoscale local structure in lead-based relaxor ferroelectrics. *Nat. Mater.* **20**, 62–67 (2021).
2. N. Izyumskaya, Y.-I. Alivov, S.-J. Cho, H. Morkoç, H. Lee, Y.-S. Kang, Processing, structure, properties, and applications of PZT thin films. *Crit. Rev. Solid State Mater. Sci.* **32**, 111–202 (2007).
3. J. M. Zaug, A. K. Soper, S. M. Clark, Pressure-dependent structures of amorphous red phosphorus and the origin of the first sharp diffraction peaks. *Nat. Mater.* **7**, 890–899 (2008).
4. J. Holoubek, H. Liu, Z. Wu, Y. Yin, X. Xing, G. Cai, S. Yu, H. Zhou, T. A. Pascal, Z. Chen, Tailoring electrolyte solvation for Li metal batteries cycled at ultra-low temperature. *Nat. Energy* **6**, 303–313 (2021).
5. G. Mao, M.-L. Saboungi, D. L. Price, M. B. Armand, W. Howells, Structure of liquid PEO-LITFSI electrolyte. *Phys. Rev. Lett.* **84**, 5536–5539 (2000).
6. X. Chen, Q. Wang, Z. Cheng, M. Zhu, H. Zhou, P. Jiang, L. Zhou, Q. Xue, F. Yuan, J. Zhu, Direct observation of chemical short-range order in a medium-entropy alloy. *Nature* **592**, 712–716 (2021).
7. R. Zhang, S. Zhao, C. Ophus, Y. Deng, S. J. Vachhani, B. Ozdol, R. Traylor, K. C. Bustillo, J. Morris, D. C. Chrzan, Direct imaging of short-range order and its impact on deformation in Ti-6Al. *Sci. Adv.* **5**, eaax2799 (2019).
8. R. Zhang, S. Zhao, J. Ding, Y. Chong, T. Jia, C. Ophus, M. Asta, R. O. Ritchie, A. M. Minor, Short-range order and its impact on the CrCoNi medium-entropy alloy. *Nature* **581**, 283–287 (2020).
9. S. Lan, L. Zhu, Z. Wu, L. Gu, Q. Zhang, H. Kong, J. Liu, R. Song, S. Liu, G. Sha, A medium-range structure motif linking amorphous and crystalline states. *Nat. Mater.* **20**, 1347–1352 (2021).
10. Y. Xie, S. Sohn, M. Wang, H. Xin, Y. Jung, M. D. Shattuck, C. S. O'Hern, J. Schroers, J. J. Cha, Supercluster-coupled crystal growth in metallic glass forming liquids. *Nat. Commun.* **10**, 1–9 (2019).
11. S. Katzoff, X-ray studies of the molecular arrangement in liquids. *J. Chem. Phys.* **2**, 841–851 (1934).

12. R. Egerton, Radiation damage to organic and inorganic specimens in the TEM. *Micron* **119**, 72–87 (2019).
13. Y. Onodera, S. Kohara, S. Tahara, A. Masuno, H. Inoue, M. Shiga, A. Hirata, K. Tsuchiya, Y. Hiraoka, I. Obayashi, Understanding diffraction patterns of glassy, liquid and amorphous materials via persistent homology analyses. *J. Ceram. Soc. Jpn.* **127**, 853–863 (2019).
14. J. Niskanen, M. Fondell, C. J. Sahle, S. Eckert, R. M. Jay, K. Gilmore, A. Pietzsch, M. Dantz, X. Lu, D. E. McNally, Compatibility of quantitative X-ray spectroscopy with continuous distribution models of water at ambient conditions. *Proc. Natl. Acad. Sci. U.S.A.* **116**, 4058–4063 (2019).
15. M. H. Nielsen, S. Aloni, J. J. De Yoreo, In situ TEM imaging of CaCO₃ nucleation reveals coexistence of direct and indirect pathways. *Science* **345**, 1158–1162 (2014).
16. E. M. Pouget, P. H. Bomans, J. A. Goos, P. M. Frederik, N. A. Sommerdijk, The initial stages of template-controlled CaCO₃ formation revealed by cryo-TEM. *Science* **323**, 1455–1458 (2009).
17. Q. Zhao, X. Liu, J. Zheng, Y. Deng, A. Warren, Q. Zhang, L. Archer, Designing electrolytes with polymerlike glass-forming properties and fast ion transport at low temperatures. *Proc. Natl. Acad. Sci. U.S.A.* **117**, 26053–26060 (2020).
18. J. Wang, Y. Yamada, K. Sodeyama, C. H. Chiang, Y. Tateyama, A. Yamada, Superconcentrated electrolytes for a high-voltage lithium-ion battery. *Nat. Commun.* **7**, 1–9 (2016).
19. Y. Yamada, A. Yamada, Review—Superconcentrated electrolytes for lithium batteries. *J. Electrochem. Soc.* **162**, A2406–A2423 (2015).
20. D. Hubble, D. E. Brown, Y. Zhao, C. Fang, J. Lau, B. D. McCloskey, G. Liu, Liquid electrolyte development for low-temperature lithium-ion batteries. *Energ. Environ. Sci.* **15**, 550–578 (2022).
21. Z. Yu, H. Wang, X. Kong, W. Huang, Y. Tsao, D. G. Mackanic, K. Wang, X. Wang, W. Huang, S. Choudhury, Molecular design for electrolyte solvents enabling energy-dense and long-cycling lithium metal batteries. *Nat. Energy* **5**, 526–533 (2020).
22. D. A. Rakov, F. Chen, S. A. Ferdousi, H. Li, T. Pathirana, A. N. Simonov, P. C. Howlett, R. Atkin, M. Forsyth, Engineering high-energy-density sodium battery anodes for improved cycling with superconcentrated ionic-liquid electrolytes. *Nat. Mater.* **19**, 1096–1101 (2020).
23. K. Kimura, H. Kiuchi, M. Morita, T. Kawaguchi, K. Yoshii, H. Sakaebe, K. Hayashi, Development of a half-cell for x-ray structural analysis of liquid electrolytes in rechargeable batteries. *Rev. Sci. Instrum.* **91**, 033907 (2020).
24. Y. Kameda, Y. Umebayashi, M. Takeuchi, M. A. Wahab, S. Fukuda, S.-I. Ishiguro, M. Sasaki, Y. Amo, T. Usuki, Solvation structure of Li⁺ in concentrated LiPF₆–Propylene carbonate solutions. *J. Phys. Chem. B* **111**, 6104–6109 (2007).
25. M. P. Foley, C. Worosz, K. Sweely, W. Henderson, H. De Long, P. C. Trulove, Phase behavior and solvation of lithium trifluoromethanesulfonate in propylene carbonate. *ECS Transactions* **45**, 41–47 (2013).
26. O. Panova, C. Ophus, C. J. Takacs, K. C. Bustillo, L. Balhorn, A. Salleo, N. Balsara, A. M. Minor, Diffraction imaging of nanocrystalline structures in organic semiconductor molecular thin films. *Nat. Mater.* **18**, 860–865 (2019).
27. K. C. Bustillo, S. E. Zeltmann, M. Chen, J. Donohue, J. Ciston, C. Ophus, A. M. Minor, 4D-STEM of beam-sensitive materials. *Acc. Chem. Res.* **54**, 2543–2551 (2021).
28. B. H. Savitzky, S. E. Zeltmann, L. A. Hughes, H. G. Brown, S. Zhao, P. M. Pelz, T. C. Pekin, E. S. Barnard, J. Donohue, L. R. DaCosta, py4DSTEM: A software package for four-dimensional scanning transmission electron microscopy data analysis. *Microsc. Microanal.* **1**–32 (2021).
29. M. J. Zachman, Z. Tu, S. Choudhury, L. A. Archer, L. F. Kourkoutis, Cryo-STEM mapping of solid–liquid interfaces and dendrites in lithium-metal batteries. *Nature* **560**, 345–349 (2018).
30. Y. Li, Y. Li, A. Pei, K. Yan, Y. Sun, C.-L. Wu, L.-M. Joubert, R. Chin, A. L. Koh, Y. Yu, Atomic structure of sensitive battery materials and interfaces revealed by cryo-electron microscopy. *Science* **358**, 506–510 (2017).
31. Z. Zhang, Y. Li, R. Xu, W. Zhou, Y. Li, S. T. Oyakhire, Y. Wu, J. Xu, H. Wang, Z. Yu, Capturing the swelling of solid-electrolyte interphase in lithium metal batteries. *Science* **375**, 66–70 (2022).
32. K.-i. Murata, H. Tanaka, General nature of liquid–liquid transition in aqueous organic solutions. *Nat. Commun.* **4**, 1–8 (2013).
33. P. Ercius, J. A. Hachtel, R. F. Klie, Chemical and bonding analysis of liquids using liquid cell electron microscopy. *MRS Bulletin* **45**, 761–768 (2020).
34. C. Brown, The crystal structure of ethylene carbonate. *Acta Crystallogr.* **7**, 92–96 (1954).
35. M. S. Ding, K. Xu, S. Zhang, T. R. Jow, Liquid/solid phase diagrams of binary carbonates for lithium batteries part II. *J. Electrochem. Soc.* **148**, A299 (2001).
36. M. Lekgoathi, L. Kock, Effect of short and long range order on crystal structure interpretation: Raman and powder X-ray diffraction of LiPF₆. *Spectrochim. Acta A Mol. Biomol. Spectrosc.* **153**, 651–654 (2016).
37. S. Lee, E. G. Teich, M. Engel, S. C. Glotzer, Entropic colloidal crystallization pathways via fluid–fluid transitions and multidimensional prenucleation motifs. *Proc. Natl. Acad. Sci. U.S.A.* **116**, 14843–14851 (2019).
38. S. Sugai, A. Onodera, Medium-range order in permanently densified SiO₂ and GeO₂ glass. *Phys. Rev. Lett.* **77**, 4210–4213 (1996).
39. N. Murthy, H. Minor, C. Bednarczyk, S. Krimm, Structure of the amorphous phase in oriented polymers. *Macromolecules* **26**, 1712–1721 (1993).
40. O. Borodin, L. Suo, M. Gobet, X. Ren, F. Wang, A. Faraone, J. Peng, M. Olguin, M. Schroeder, M. S. Ding, Liquid structure with nano-heterogeneity promotes cationic transport in concentrated electrolytes. *ACS Nano* **11**, 10462–10471 (2017).
41. Y. Yamada, J. Wang, S. Ko, E. Watanabe, A. Yamada, Advances and issues in developing salt-concentrated battery electrolytes. *Nat. Energy* **4**, 269–280 (2019).
42. J.-H. Choi, H. Lee, H. R. Choi, M. Cho, Graph theory and ion and molecular aggregation in aqueous solutions. *Annu. Rev. Phys. Chem.* **69**, 125–149 (2018).
43. Y. Yamada, K. Furukawa, K. Sodeyama, K. Kikuchi, M. Yaegashi, Y. Tateyama, A. Yamada, Unusual stability of acetonitrile-based superconcentrated electrolytes for fast-charging lithium-ion batteries. *J. Am. Chem. Soc.* **136**, 5039–5046 (2014).
44. O. Borodin, J. Self, K. A. Persson, C. Wang, K. Xu, Uncharted waters: Super-concentrated electrolytes. *Joule* **4**, 69–100 (2020).
45. C. Li, R. Kingsbury, L. Zhou, A. Shyamsunder, K. A. Persson, L. F. Nazar, Tuning the solvation structure in aqueous zinc batteries to maximize Zn-ion intercalation and optimize dendrite-free zinc plating. *ACS Energy Lett.* **7**, 533–540 (2022).
46. S. C. DeCaluwe, J. A. Dura, Finite thickness effects on nafion water uptake and ionic conductivity at hydrophilic substrate interfaces, and implications for PEMFC performance. *ECS Transactions* **80**, 619–632 (2017).
47. A. P. Thompson, H. M. Aktulga, R. Berger, D. S. Bolintineanu, W. M. Brown, P. S. Crozier, P. J. in't der Veld, A. Kohlmeyer, S. G. Moore, T. D. Nguyen, LAMMPS—a flexible simulation tool for particle-based materials modeling at the atomic, meso, and continuum scales. *Comput. Phys. Commun.* **271**, 108171 (2022).
48. G. A. Kaminski, R. A. Friesner, J. Tirado-Rives, W. L. Jorgensen, Evaluation and reparameterization of the OPLS-AA force field for proteins via comparison with accurate quantum chemical calculations on peptides. *J. Phys. Chem. B* **105**, 6474–6487 (2001).
49. J. N. Canongia Lopes, A. A. Pádua, Molecular force field for ionic liquids composed of triflate or bistriflylimide anions. *J. Phys. Chem. B* **108**, 16893–16898 (2004).
50. S. V. Sambasivarao, O. Acevedo, Development of OPLS-AA force field parameters for 68 unique ionic liquids. *J. Chem. Theory Comput.* **5**, 1038–1050 (2009).
51. W. L. Jorgensen, D. S. Maxwell, J. Tirado-Rives, Development and testing of the OPLS all-atom force field on conformational energetics and properties of organic liquids. *J. Am. Chem. Soc.* **118**, 11225–11236 (1996).
52. L. Martínez, R. Andrade, E. G. Birgin, J. M. Martínez, PACKMOL: A package for building initial configurations for molecular dynamics simulations. *J. Comput. Chem.* **30**, 2157–2164 (2009).
53. N. Michaud-Agrawal, E. J. Denning, T. B. Woolf, O. Beckstein, MDAnalysis: A toolkit for the analysis of molecular dynamics simulations. *J. Comput. Chem.* **32**, 2319–2327 (2011).
54. A. Stukowski, Visualization and analysis of atomistic simulation data with OVITO—The Open Visualization Tool. *Model. Simul. Mater. Sci. Eng.* **18**, 015012 (2009).
55. R. D. Leapman, S. Sun, Cryo-electron energy loss spectroscopy: Observations on vitrified hydrated specimens and radiation damage. *Ultramicroscopy* **59**, 71–79 (1995).

Acknowledgments: We thank M. Ding from Army Research Laboratory for the valuable discussion on glass transition temperature of electrolyte. We thank M. Liu for Fig. 1 design.

Funding: This work was supported by the U.S. Department of Energy (DOE), Office of Science, Office of Basic Energy Sciences (BES), Materials Science and Engineering Division under contract no. DE-AC02-05-CH11231 within the KC22ZH program. Work at the Molecular Foundry was supported by the Office of Science, Office of Basic Energy Sciences, of the U.S. Department of Energy under contract no. DE-AC02-05CH11231. The theoretical part of work was supported by the DOE BES funded KCD252 program. B.H.S. received support from the Toyota Research Institute. **Author contributions:** Y.X., P.E., and H.Z. conceived the project. Y.X. designed the experiments. Y.X. conducted the TEM experiments with the help from K.B. Y.X., C.O., P.E., and B.H.S. analyzed the experimental data. Z.C. and Y.X. performed machine learning analyses. J.W. conducted the MD simulation and related analysis under the supervision of L.-W.W. and K.P. Y.X. and J.W. drafted the manuscript. All authors discussed the results and edited the manuscript. **Competing interests:** The authors declare that they have no competing interests. **Data and materials availability:** All data needed to evaluate the conclusions in the paper are present in the paper and/or the Supplementary Materials.

Submitted 12 May 2022
 Accepted 16 December 2022
 Published 13 January 2023
 10.1126/sciadv.adc9721

Spatially resolved structural order in low-temperature liquid electrolyte

Yujun Xie, Jingyang Wang, Benjamin H. Savitzky, Zheng Chen, Yu Wang, Sophia Betzler, Karen Bustillo, Kristin Persson, Yi Cui, Lin-Wang Wang, Colin Ophus, Peter Ercius, and Haimei Zheng

Sci. Adv., **9** (2), eadc9721.

DOI: 10.1126/sciadv.adc9721

View the article online

<https://www.science.org/doi/10.1126/sciadv.adc9721>

Permissions

<https://www.science.org/help/reprints-and-permissions>

Use of this article is subject to the [Terms of service](#)

Science Advances (ISSN) is published by the American Association for the Advancement of Science. 1200 New York Avenue NW, Washington, DC 20005. The title *Science Advances* is a registered trademark of AAAS.

Copyright © 2023 The Authors, some rights reserved; exclusive licensee American Association for the Advancement of Science. No claim to original U.S. Government Works. Distributed under a Creative Commons Attribution NonCommercial License 4.0 (CC BY-NC).